PAPER

Check for updates

Impact of Ni(II) coordinatively unsaturated sites and coordinated water molecules on SO₂ adsorption by a MOF with octanuclear metal clusters†

Juan L. Obeso, [iD] ‡[ab] Karuppasamy Gopalsamy,‡[c] Mohammad Wahiduzzaman,‡[c] Eva Martínez-Ahumada,[b] Dong Fan,[c] Hugo A. Lara-García, [iD] [d] Francisco J. Carmona,[e] Guillaume Maurin, [iD] *[c] Ilich A. Ibarra [iD] *[bf] and Jorge A. R. Navarro [iD] *[e]

A Ni-based pyrazolate MOF (NiBDP) is studied for SO₂ adsorption under static conditions, demonstrating a high SO₂ uptake of 8.48 mmol g⁻¹ at 298 K and 1 bar while maintaining a high chemical stability. The influence of Ni(II) coordinatively unsaturated metal sites and coordinated water on the SO₂ adsorption performance of this MOF is investigated by using a combination of experimental techniques, including FTIR and *in situ* DRIFTS measurements, along with Density Functional Theory calculations. The pore-filling of the SO₂ adsorbates within the material, at the molecular level, is further unravelled through grand Canonical Monte Carlo simulations employing a newly DFT-derived accurate set of force field parameters.

aInstituto Politécnico Nacional, Centro de Investigación en Ciencia Aplicada y Tecnología Avanzada, LNAgua, Legaria 694, Col. Irrigación, Miguel Hidalgo, 11500, CDMX, Mexico

bLaboratorio de Fisicoquímica y Reactividad de Superficies (LaFReS), Instituto de Investigaciones en Materiales, Universidad Nacional Autónoma de México, Circuito Exterior s/n, CU, Coyoacán, 04510, Ciudad de México, Mexico. E-mail: argel@unam.mx

cICGM, Univ. Montpellier, CNRS, ENSCM, Montpellier, 34293, France. E-mail: guillaume.Maurin1@umontpellier.fr

dInstituto de Física, Universidad Nacional Autónoma de México, Circuito Exterior s/n, CU, Coyoacán, 04510, Ciudad de México, Mexico

eDepartamento de Química Inorgánica, Universidad de Granada, Av. Fuentenueva S/N, Granada, 18071 Spain. E-mail: jarn@ugr.es

fOn Sabbatical as "Catedra Dr Douglas Hugh Everett" at Departamento de Química, Universidad Autónoma Metropolitana-Iztapalapa, San Rafael Atlixco 186, Col. Leyes de Reforma 1ra Seccion, Iztapalapa, C.P. 09310, Ciudad de México, Mexico

† Electronic supplementary information (ESI) available: Instrumental techniques and characterization. See DOI: https://doi.org/10.1039/d3ta07582f

‡ These authors contributed equally to this manuscript.

Introduction

The standard families of porous materials, *e.g.*, activated carbons, zeolites, and mesoporous silica, have been extensively studied for the adsorption of small molecules within their porous cavities for diverse applications.[1,2] More recently, metal–organic frameworks (MOFs), constructed by metal-containing nodes and organic linkers,[3] which can propagate in one to three dimensions, have been shown to represent a milestone in the capture of greenhouse (CH_4 and CO_2)[4-11] and toxic gases (NH_3, NO_x and SO_2).[12,13] The diversity of metal ions and organic ligands that can be used for the construction of MOFs facilitates their architecture design and, hence, the modulation of chemical features in the pore walls (*e.g.*, functionalization) and of pore dimension/shape to optimize the interactions with a given guest molecule.[14] Therefore, a selection of MOFs has emerged as promising candidates in the field of material science for the adsorption of toxic and corrosive gases.[15] Typically, SO_2 has gained a lot of interest since it is the main precursor of acid rain, and the hazardous effects of SO_2 on the environment and on human health are a huge concern. Thus, SO_2 capture by MOFs has been investigated since 2008, when Yaghi *et al.*,[16] reported the SO_2 adsorption by several MOFs with diverse chemical and structural features. After two decades of worldwide efforts, certain chemical characteristics have been recognized to render MOF materials not only resistant to SO_2 exposure but also with attractive capture performance.[17-19] These included the use of (i) high valent-metal ions, such as Zr^{4+}, Al^{3+}, In^{3+}, and Sc^{3+} with carboxylate ligands; (ii) robust metal clusters with strong metal–ligand bonds, for example, the use of pyrazolate or imidazolate ligands and late transition M^{2+} ions; and (iii) the inclusion of coordinately unsaturated metal sites (CUS) or functional groups (X–H), capable of interacting with SO_2 by coordination bonds,[20] hydrogen bonds,[21] and other supramolecular interactions.[22]

Nickel(II)-based MOFs are *a priori* attractive sorbents owing to the good abundance of this metal and their usually high thermal and chemical stabilities. Moreover, from a chemical point of view, Ni-based compounds are known to exhibit interesting properties such as electrocatalytic capabilities,[23] magnetic properties,[24] energy storage,[25] and detection.[26] Although some M^{2+}-based MOFs are considered unstable to SO_2

This journal is © The Royal Society of Chemistry 2024

J. Mater. Chem. A, 2024, **12**, 10157–10165 | **10157**

adsorption, the combination of polyazolate ligands and divalent metals increases the MOF structural stability over alkaline or acidic environments.[27] MOFs formed by strong Ni^{2+}–N(azolate) bonds provide greater chemical and thermal stability compared to their carboxylate analogues. According to Pearson's hard–soft acid–base principle, a highly chemically stable MOF material can be constructed using azolate ligands with low-valent transition metals. The pK_a value for the deprotonation of N–H bonds shows high structure robustness.[28] These characteristics make attractive the study of Ni^{2+} pyrazolate-based MOFs for the adsorption of corrosive gases.[29]

Herein, we investigate a Ni(II)-based MOF, $[Ni_8(OH)_4(H_2O)_2(BDP)_6]$ termed NiBDP (H_2BDP = 1,4-bis(pyrazol-4-yl) benzene), for SO_2 capture. This material is based on octanuclear Ni(II) hydroxo clusters $[Ni_8(OH)_4(H_2O)_2]$, linked by BDP to form $[Ni_8(OH)_4(H_2O)_2(BDP)_6]$ cluster (Fig. 1a). NiBDP material, along with an isoreticular series of MOFs, has been studied earlier for dynamic breakthrough SO_2 adsorption.[30] Results showed an SO_2 uptake of 2.02 mmol g^{-1} at 303 K, and cycling experiments revealed a reversible physisorption process.

Although this Ni(II)-based MOF was previously investigated under SO_2 (dynamic breakthrough), we decided to explore its SO_2 adsorption capacities under static condition at room temperature and 1 bar, in order to gain a comprehensive understanding on the SO_2 adsorption mechanism. Also, neither experimental exploration in thermodynamic conditions nor a complete understanding of the microscopic mechanism in play have been reported so far in the literature. Thus, we have embarked on the task of coupling advanced experimental and theoretical approaches to revisit the SO_2 adsorption performance of NiBDP in static mode and gain a full picture of the adsorption mechanism at the molecular level. A special attention has been also paid to assess computationally the impact of coordinated water on the SO_2 adsorption isotherms by considering different NiBDP-nH_2O structures (where n = 0, 1, 2, correspond to distinct structure models possessing 100%, 50%, and zero CUS sites per metal node) that mimic scenarios of full,

partial or non-evacuation of the CUS sites during the experimental activation of the sample.

Experimental

Synthesis of NiBDP

NiBDP was synthesized according to the reported procedure.[31] In a typical synthesis, 63.1 mg (0.3 mmol) of 4,4′-benzene-1,4-diylbis(1H-pyrazole) (H_2BDP) were dissolved in 16 mL of DMF, and 99.2 mg (0.4 mmol) of $Ni(AcO)_2 \cdot 4H_2O$ were dissolved in 4 mL of H_2O. The two limpid solutions were mixed and refluxed for 6 h under stirring. The light green solid obtained was filtered and washed with EtOH and Et_2O, yielding 89 mg (66%). IR (KBr) 3433(br), 1655(vs.), 1574(s), 1390(m), 1358(m), 1250(s), 1182(w), 1124(w), 1057(s), 958(s), 845(m), 658(w), 540(w), 505(w) cm^{-1}.

Characterization methods

Detailed information on the instrumental techniques is available in the ESI: Section S1.†

SO_2 sorption measurements

SO_2 adsorption–desorption isotherms were measured in a Dynamic Gravimetric Gas/Vapour Sorption Analyser, DVS vacuum (Surface Measurement Systems Ltd) with a static method. The samples were activated at 423 K under vacuum (1 × 10^{-6} bar) for 5 hours. SO_2 adsorption isotherm was carried out at 298 K up to 1 bar.

DFT geometry optimization

Periodic DFT calculations were conducted to optimize the atomic position and cell volume of both the empty NiBDP-nH_2O structures (where n = 0, 1, 2, correspond to different structure models possessing 100%, 50%, and zero CUS sites per metal node) and the associated guest-loaded structures with SO_2 adsorbed onto them using Vienna Ab initio Simulation Package (VASP).[32] The core and valence electrons of the interacting elements were treated with projector-augmented-wave (PAW) potentials and plane-wave basis sets.[33] The general gradient approximation (GGA) to the exchange–correlation functional according to Perdew–Burke–Ernzerhof (PBE)[34] was used along with a combination of Grimme's empirical dispersion correction with Becke–Johnson damping (DFT-D3/BJ).[35] To account for the electronic correlation of d electrons on-site, Hubbard U correction was considered for Ni(II) atoms, with the benchmark U value of 6.4 eV previously validated on different properties of Ni(II) oxide systems as well as Ni(II) MOFs.[36–38] Γ point meshes for sampling the Brillouin zone were used along a plane-wave kinetic energy cutoff of 520 eV. The energy and ionic force convergence criteria were set to 1 × 10^{-6} eV and 0.02 eV $Å^{-1}$, respectively. Consequently, the atomic partial charges of the MOF atoms of the DFT-optimized empty MOF structures were derived by employing the density-derived electrostatic and chemical (DDEC) charge partitioning scheme as implemented in the chargemol program.[39,40] These atomic partial charges are provided in Table S1 in the ESI.† The textural properties of NiBDP-nH_2O (n = 0, 1, 2) MOFs, including pore volume (PV),
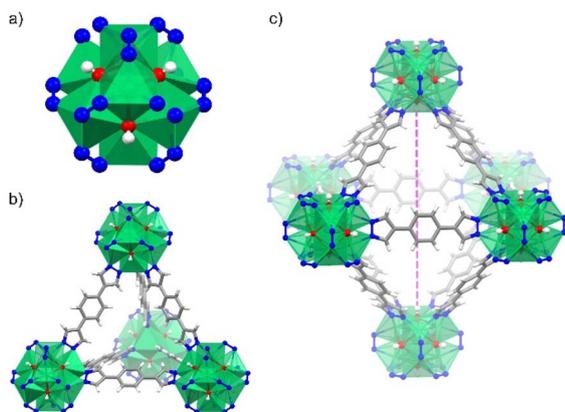

Fig. 1 (a) Structure of the octanuclear Ni(II) cluster in $[Ni_8(OH)_4(H_2O)_2(BDP)_6]$. (b) View of the tetrahedral, and (c) octahedral cages found in the crystal structure of NiBDP MOF. Color code: Ni (green); N (blue); O (red); C (grey) and H (white).

10158 | J. Mater. Chem. A, 2024, **12**, 10157–10165

This journal is © The Royal Society of Chemistry 2024

surface area (SA), largest cavity diameter (LCD) and pore limiting diameter (PLD), were calculated by using Zeo++ software (see details for the calculations in the ESI†),[41] and tabulated in Table S2.†

Force field parameterization

The consideration of generic force field for MOF frameworks combined with force field models for the guest molecules is known to dramatically fail to describe specific interactions between coordinative unsaturated MOFs with any guest molecules.[42–46] Therefore, such MOF- CUS sites/guest molecule interactions require a specific FF parameterization based on first-principle quantum calculations. To do so, a 100% CUS containing model of the NiBDP MOF (*i.e.*, NiBDP-0H$_2$O) was first considered and an approaching path consisting of 10 different configurations associated to different SO$_2$–Ni CUS (NiBDP-0H$_2$O) separating distances were constructed while maintaining the same orientation as DFT-optimized minimum energy structure (Fig. S9†). Subsequently, single point energy calculations were performed to deduce the corresponding interaction energies for a SO$_2$ molecule within the NiBDP-0H$_2$O pore using the energy expression: $E_{int} = E_{NiBDP-0H_2O+SO_2} - (E_{NiBDP-0H_2O} + E_{SO_2})$, where, $E_{NiBDP-0H_2O+SO_2}$ corresponds to the single point energies of the SO$_2$ loaded NiBDP-0H$_2$O adsorption configurations along the interacting path, while $E_{NiBDP-0H_2O}$ and E_{SO_2} correspond to the energy associated to an empty NiBDP-0H$_2$O MOF and an isolated SO$_2$ molecule, respectively. The resulting interaction energy curve was then fitted to an analytical function combining van der Waals (vdW) and coulombic terms. Here, nonbonded interactions between SO$_2$ and NiBDP-0H$_2$O MOF atoms other than Ni(II) sites were modeled with standard Lennard-Jones (LJ) 12-6 potential while a Morse potential was employed to describe the interactions between SO$_2$ and Ni(II) atoms. The LJ parameters (ε and σ) for the MOF atoms were adopted from the universal force field (UFF),[47] whereas the SO$_2$ molecule was represented by the three-site LJ charged model reported by Ketko *et al.*,[48] (Tables S3–S5†). LJ cross-terms were then calculated using the Lorentz–Berthelot combination rules. The Ewald summation technique[49] was employed to compute the long-range coulombic contributions, in which, the atomic partial charges of the MOF are determined using the DDEC charge partitioning scheme as mentioned above, while the charges for SO$_2$ are obtained from the potential model of Ketko *et al.*[48] Finally, the Morse potential parameters, D, α, and r_0 associated with the Ni(II)–O(SO$_2$)– and Ni(II)–S(SO$_2$) specific interactions were determined using the General Utility Lattice Program (GULP)[50] by minimizing the energy differences with respect to the DFT counterpart. The corresponding fitting curve and the parameters are available in the ESI.†

Monte Carlo simulations

The SO$_2$ adsorption isotherms for all three NiBDP-nH$_2$O ($n = 0$, 1, 2) structures were calculated through the GCMC simulations implementing the force field discussed above using the Complex Adsorption and Diffusion Simulation Suite (CADSS) of the program.[42] Nonetheless, for the NiBDP-2H$_2$O structure, the SO$_2$ adsorption isotherm was computed by using generic UFF parameters for all framework atoms, as the system does not contains any CUS sites. We employed a simulation box comprising eight-unit cells ($2 \times 2 \times 2$) of the MOFs. The atomic positions of the MOFs' skeletons were held fixed during the adsorption, and Monte Carlo trial moves for the guest molecules. The host–guest nonbonded interactions were computed in real space using a cutoff of 12.0 Å. The long-range electrostatic interactions were calculated using the Ewald summation technique[49] with an accuracy of 1×10^{-6}. For each pressure point, 1×10^7 and 2×10^7 Monte Carlo steps including insertion/deletion, translation and rotational moves, were considered for equilibration and production, respectively. The Peng–Robinson equation of state was used to determine the gas-phase fugacity for SO$_2$ molecules.[51] The overall adsorption isotherms were obtained by running GCMC simulations for different fugacities ranging from 10^{-4} to 1 bar. Additionally, the enthalpy of SO$_2$ adsorption at infinite dilution was computed employing Widom's test particle insertion method.[52]

Results and discussion

Characterization of NiBDP

NiBDP MOF was synthesized according to the reported procedure.[31] This structure crystallizes in the face cubic centered (fcu) topology with the $Fm\bar{3}m$ space group. Each Ni(II) ion is bonded to three N atoms from different organic linkers, and three of the six μ_4-O observed in the octanuclear cluster (Fig. 1a). It is important to note that two of the six oxygen atoms belong to coordinated water molecules rather than hydroxo ligands.[53] The structure contains two types of cages: an octahedral cage (diameter of $\sim$16 Å) connecting to eight tetrahedral cages (diameter of $\sim$9 Å) accessible *via* triangular windows (diameter of $\sim$6 Å), (Fig. 1b, c and S1†). In the octahedral cage, the OH groups point toward the centre of the pore, which can favor interactions with SO$_2$ in addition to the Ni(II) sites, as it was demonstrated for other materials, such as the MFM-300 family.[54] The crystalline structure was confirmed by PXRD (Fig. S2†). Based on N$_2$ sorption measurements at 77 K (Fig. S3†), the activated NiBDP shows a BET surface area of 1220 m^2 g^{-1}, which is lower than the previously reported (1730 m^2 g^{-1}).[55] The corresponding theoretically calculated surface areas of NiBDP_0H$_2$O and NiBDP_2H$_2$O are 2650 m^2 g^{-1} and 2480 m^2 g^{-1}, respectively, suggesting that the CUS sites of the investigated sample are not fully evacuated. In addition, elemental analysis (EA) of NiBDP (Ni$_8$(OH)$_4$(H$_2$O)$_2$(BDP)$_6$](H$_2$O)$_2$(DMF)$_{10}$) was conducted. Anal. calc. for NiBDP (2589.90 g mol^{-1}) C, 47.3; H, 5.06; N, 18.4; Ni, 18.1, found C, 46.7; H, 5.10; N, 18.2; Ni, 18.8. Nickel content was determined on the basis of TGA (Fig. S4†). Also, electronic spectra (Fig. S5†) characterization is indicative of the presence of the characteristic d–d transition bands of Ni(II) in a poorly distorted Oh environment ($^3T_{2g}$(F) $\leftarrow$ $^3A_{2g}$(F), 10 350 cm^{-1}; $^3T_{1g}$(F) $\leftarrow$ $^3A_{2g}$(F), 15 870 cm^{-1}; $^3T_{1g}$(P) $\leftarrow$ $^3A_{2g}$(F), 25 800 cm^{-1}).

SO$_2$ sorption in NiBDP

Previously, the SO$_2$ capture in NiBDP was reported using breakthrough experiments for an N$_2$/SO$_2$ mixture. However,

This journal is © The Royal Society of Chemistry 2024

J. Mater. Chem. A, 2024, **12**, 10157–10165 | **10159**

under these conditions, a relatively low SO_2 concentration (P_{SO_2} = 0.025 bar) was considered. NiBDP showed a total uptake of 2.02 mmol g^{-1} at 303 K. The SO_2 affinity was attributed to the Lewis acid–base interactions with crystal defects.[30] However, equilibrium adsorption–desorption isotherms are more appropriate to gain deep insights into the adsorption capacity, adsorption mechanism and to understand the adsorption behavior of certain gases within a porous material.[56] Thus, the SO_2 adsorption–desorption isotherms were investigated for NiBDP. The corresponding SO_2 sorption isotherm is shown in Fig. 2. A steep profile is observed in the adsorption isotherm from 0 to 0.025 bar. At this stage, SO_2 adsorption reaches a value of 1.85 mmol g^{-1} and remains almost constant up to 0.45 bar (1.89 mmol g^{-1}). This SO_2 uptake is similar to that reported so far for other MOFs like MFM-133 (1.2 mmol g^{-1}),[57] MFM-422 (1.8 mmol g^{-1}),[57] SIFSIX-3-Zn (1.89 mmol g^{-1}),[58] and ELM-12 (1.95 mmol g^{-1})[59] at 0.1 bar implying that NiBDP can be used as an alternative SO_2 adsorbent at low gas pressures. Interestingly, a sharp jump in the SO_2 adsorption capacity from 1.89 mmol g^{-1} up to 7.22 mmol g^{-1} is observed at 0.45 bar, which ultimately reaches a total SO_2 uptake of 8.48 mmol g^{-1} at 1 bar. The latter value is comparable to a variety of MOF materials such as UiO-66-Cu,[57] MFM-300(In)[60] and MIL-53(Al)-TDC[61] with a reported SO_2 uptake of 8.2 mmol g^{-1}, 8.28 mmol g^{-1}, and 8.9 mmol g^{-1}, respectively, under similar working conditions (1 bar and 298 K). Considering the experimental BET surface area of NiBDP (1220 m^2 g^{-1}), the SO_2 uptake of 8.48 mmol g^{-1} aligns well with other microporous MOFs with similar surface area, for instance, UiO-66, possessing the same fcu topology and a BET surface area of 1221 m^2 g^{-1}, can adsorb 8.6 mmol g^{-1} of SO_2 at 298 K and 1 bar.[57]

Interestingly, the adsorption isotherm profile is unusual for a well-defined microporous MOF. In the low-pressure region, a rapid adsorption profile is defined, which can be related to a high interaction between the Ni^{2+} CUS sites and the SO_2

molecule, which can be postulated as a possible main adsorption site for NiBDP and gives rise to adsorbate seeding in the pore structure.[61] Then, a subsequent almost horizontal plateau is observed, which can be associated with the presence of weaker interaction sites such as water molecules and hydroxide groups coordinated to the Ni^{2+} sites. Later, the sudden step at 0.45 bar followed by a linear adsorption (SO_2 saturation up to 1 bar) should be related to an adsorbate clustering, giving rise to pore filling. The observed seeding and clustering adsorption behavior can be related to the water adsorption mechanism unraveled for the MOF-303 system.[62]

Finally, the retention of NiBDP crystallinity after SO_2 adsorption was corroborated by PXRD analysis (Fig. S2†), demonstrating that the inclusion of polyazolate-containing ligands and borderline soft acid Ni^{2+} in MOFs improves their structural stability against corrosive gases.[63]

Furthermore, the isosteric enthalpy of adsorption (ΔH) for SO_2 adsorption was calculated at low coverage using the virial method (Fig. S6†).[64] The calculated value at low SO_2 loading (<0.03 bar) is −41.2 kJ mol^{-1}, which is in good agreement with the value reported in earlier (−40.1 kJ mol^{-1}).[30] This relatively high value can be associated with moderately strong SO_2 interaction with NiBDP. Typically, a MOF material with CUS sites usually shows a high ΔH value (−80/−90 kJ mol^{-1}) due to the strong coordination between the metal and the SO_2 molecule.[26] The lower value obtained here can be related to a decrease in the availability of Ni^{2+} CUS sites due to the presence of coordinated water.

FTIR and DRIFTS analysis in NiBDP

FTIR experiments were carried out on a NiBDP sample before and after exposure to SO_2 gas and moisture traces to confirm the stability (Fig. S7†). The FTIR spectra of NiBDP show the characteristic bands for a pyrazolate MOF material. The bands related to C=O and C=C are associated with the peaks at 1649 and 1574 cm^{-1}, respectively.[65] The bands at 1410 and 1385 cm^{-1} are related to C=N. The bands at 1240 and 510 cm^{-1} are assigned to N–N bonds in the organic linker and the coordination bonds between Ni and N, respectively.[66] Also, after SO_2 adsorption show different bands from the region 1800–450 cm^{-1} (Fig. 3a). Two principal SO_2 bands at 1153 cm^{-1} and 1303 cm^{-1} are observed, that are related to asymmetric and symmetric stretching modes of SO_2 molecules within the pores. This type of interaction agrees with SO_2 physisorption on Ni(BDC)(TED)$_{0.5}$ with bands at 1144 and 1326 cm^{-1}.[67] Finally, the formation of hydrolyzed species of SO_2 (i.e., SO_3^{2-} or HSO_3^{2-}) due to the presence of water is discarded due to the lack of characteristic IR bands for these ions.

In addition, in situ DRIFTS measurements were conducted using CO as a probe molecule. This technique is a powerful tool to characterise acid/base sites for different porous materials, including MOFs.[68] Even though the chemical nature of CO is different to SO_2, this study is useful to gain insight into the possible adsorption sites for the guest molecules, as previously reported[69] in particular to make the distinction between the interactions with Ni^{2+} CUS sites or the coordinated water

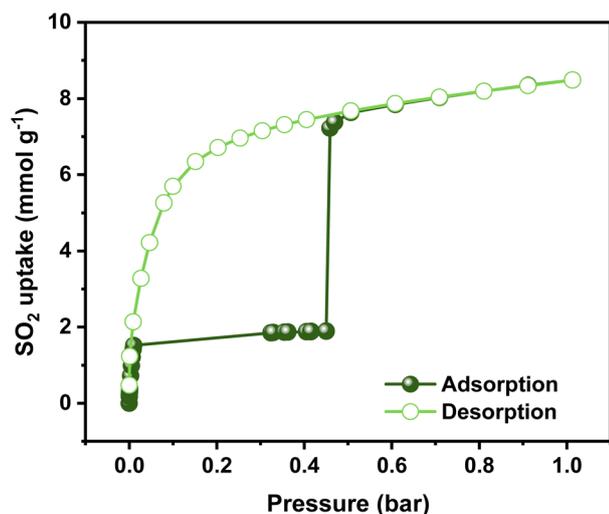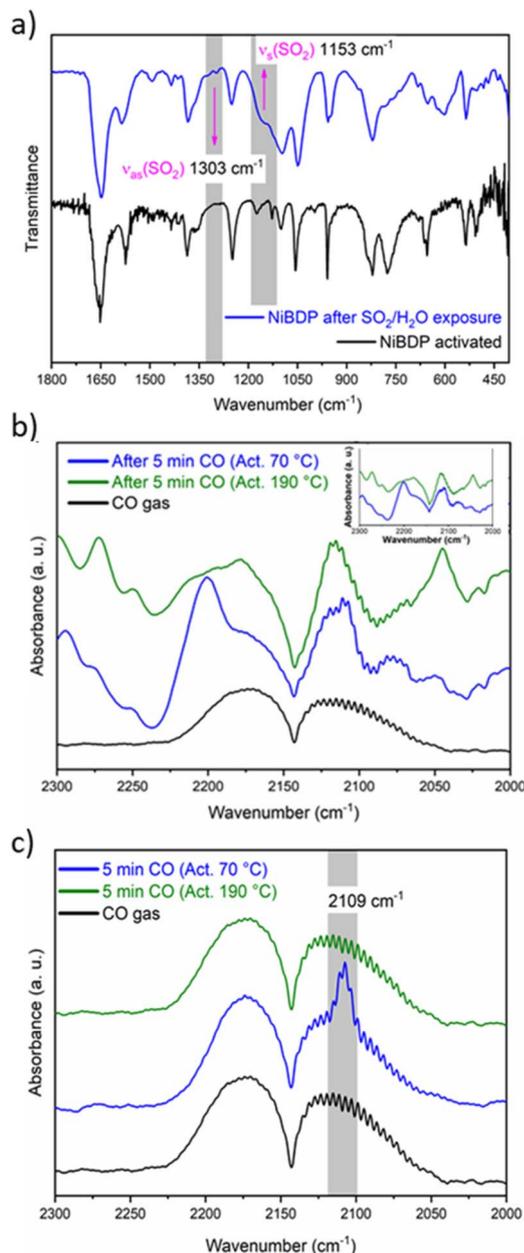
Fig. 2 Experimental SO_2 adsorption–desorption isotherm of an activated NiBDP sample (filled green circles = adsorption; open green circles = desorption) at 298 K up to 1 bar.

10160 | J. Mater. Chem. A, 2024, 12, 10157–10165

This journal is © The Royal Society of Chemistry 2024

Fig. 3 (a) FT-IR spectra of activated and SO_2-loaded NiBDC material, into 1800–400 cm^{-1} wavelength region. Gray rectangles show the asymmetric ν_{as} and symmetric ν_s stretch modes of physically adsorbed SO_2 molecules. (b) IR spectra on activated NiBDP at 70 °C (blue line) and 190 °C (green line) in the region between 2300 and 2000 cm^{-1} after 5 min of CO flux. (c) Subtracted spectra before and after admittance of CO in the region between 2300 and 2000 cm^{-1} after 5 min of CO flux.

molecules. Herein, the CO adsorption was studied by DRIFTS *in situ* analysis at 298 K after sample activation at two different temperatures, 70 and 190 °C under a He atmosphere.

The IR spectra of the activated sample are shown in Fig. S8.† When the sample was activated at 70 °C, broadband was observed between 3450 and 3200 cm^{-1}. On the other hand, when the sample was activated at 190 °C, this band partially

decreased in intensity. This band is associated with water molecules that are not fully desorbed from the Ni^{2+} centers. Fig. 3b shows the spectra after 5 min of a continuous CO flux. The CO gas spectrum is composed of two asymmetric peaks centered at 2173 and 2113 cm^{-1}. When the CO is absorbed by the MOF, these two peaks are also observed, but the shape changes. The principal difference between the samples activated at 70 °C and 190 °C seems to be a peak depicted at 2200 cm^{-1}. However, compared to the blank spectra (Fig. 3b, inset), it is observed that this peak belongs to the sample.

To analyze the difference in CO adsorption between the two activation methods, a subtraction of the spectra before and after the admittance of CO was carried out. Fig. 3c shows the subtracted spectra. It is evident that a peak appears at 2109 cm^{-1} when the sample is activated at 70 °C. This peak was already assigned to the adsorption of CO over metallic Ni.[70] Therefore, the DRIFT analysis confirms that both Ni^{2+} CUS sites and coordinated water can interact with the guest molecules in activated NiBDP sample.

SO_2 adsorption simulations

To further gain insights into the effect of Ni^{2+} CUS sites and coordinated water molecules in the SO_2 adsorption, the adsorption of SO_2 in NiBDP with and without evacuated Ni(II) CUS sites were systematically studied through GCMC simulations to fully understand the resulting adsorption behavior. As a starting point, we computed the SO_2 single component adsorption isotherm for NiBDP-2H$_2$O MOF at 298 K, covering a pressure range from 1×10^{-4} to 1 bar, and by using the generic UFF potential parameters as the system does not contain CUS sites. As illustrated in Fig. 4, our GCMC simulations result in an SO_2 uptake of 15.2 mmol g^{-1} for this NiBDP-2H$_2$O structure at 1 bar, which exceeds the experimentally determined maximum uptake of 8.48 mmol g^{-1}. This deviation
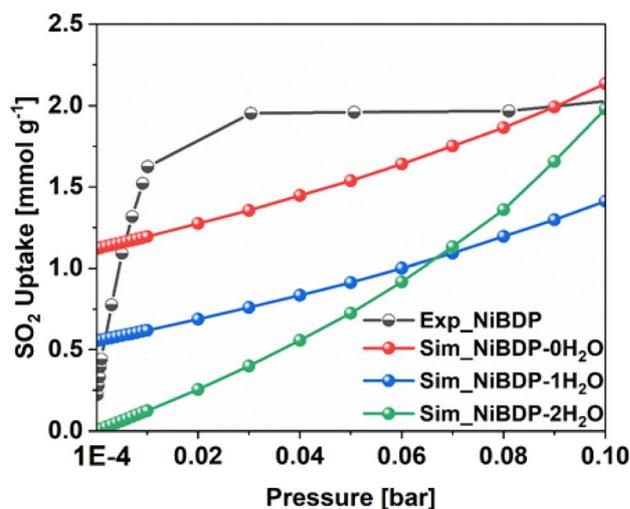
Fig. 4 Comparison of SO_2 adsorption isotherms in NiBDP MOFs, obtained experimentally and calculated by GCMC simulations at 298 K for 3 different structure models containing 0, 1 or 2 water molecules per unit cell, covering a pressure range from 1×10^{-4} to 1 bar.

This journal is © The Royal Society of Chemistry 2024

J. Mater. Chem. A, 2024, **12**, 10157–10165 | **10161**

is expected due to the difference in the experimental BET surface area (1220 m^2 g^{-1}) and theoretical N$_2$ surface area (NiBDP_0H$_2$O and NiBDP_2H$_2$O of 2650 m^2 g^{-1} and 2484 m^2 g^{-1}, respectively).

This discrepancy further underscores the ambiguity about the proper activation of CUS-containing MOFs, where the number of weakly coordinated water molecules removed from the framework and the creation of CUS sites can vary significantly, influenced by specific experimental conditions and activation procedures. CUS sites are considered the most attractive and predominant adsorption sites for all types of approaching guest molecules, especially under very low-pressure conditions. To further assess the influence of CUS sites present within the NiBDP framework on its SO$_2$ uptake performance, we further considered two model systems, namely NiBDP-1H$_2$O (with 50% CUS sites, i.e., one H$_2$O per metal node) and NiBDP-0H$_2$O (with 100% CUS sites, no H$_2$O on the metal nodes). In the literature, it has been widely debated that generic force fields such as UFF[47] and DREIDING[71] are not capable of accurately predicting the strong host–guest interactions in MOFs containing CUS sites.

Therefore, in the current study, we derived a specific set of Morse type potential parameters through periodic DFT calculations to accurately assess the strength of the pair-wise SO$_2$–Ni(II) CUS sites interactions using the 100% CUS containing NiBDP-0H$_2$O model (see parametrization details in the experimental section). Notably, DFT determined minimum energy geometry of SO$_2$ adsorption configuration in NiBDP-0H$_2$O framework reveals that an SO$_2$ molecule interacts with four Ni(II) open metal sites through an oxygen atom, with characteristic separation distances ranging from 2.27 to 2.49 Å (Fig. S10†), accompanied by a DFT-derived binding energy of −118.6 kJ mol^{-1}. As also depicted in Fig. S10,† the second oxygen atom of the SO$_2$ molecule was found to be oriented toward the nitrogen atom of the MOF framework, maintaining a separation distance of 2.93 Å.

Consequently, GCMC simulations performed utilizing our newly DFT-derived SO$_2$/Ni(II) force fields effectively reproduce the characteristic SO$_2$–Ni(II) interacting distances (see Fig. 5a) observed in the DFT equilibrium geometry as demonstrated in the corresponding radial distribution function (RDF) plots calculated under low-pressure conditions (Fig. 6a, S11 and S12†). The steep simulated uptake of SO$_2$ in NiBDP-0H$_2$O at the very initial stage of adsorption (Fig. 4) corresponds to the initial binding of each Ni(II) site by 1SO$_2$ molecule as illustrated in Fig. 5a with a characteristic interacting Ni–O(SO$_2$) distance of 2.5 Å (as shown by the RDF plotted in Fig. 6a). Fig. 6b evidence an additional interaction between the second oxygen of SO$_2$ with framework nitrogen atoms (Fig. S10†), the corresponding calculated RDFs between N–O(SO$_2$) and N–S(SO$_2$) showing peaks at 2.9 Å and 3.2 Å, respectively. This dual-site adsorption mode is probably the origin of the overestimation of the experimental adsorption uptake in the very low domain of pressure.

Second, Fig. 5 illustrates that at a moderate pressure range, SO$_2$ molecules predominantly populate the region in the vicinity of the organic ligands, giving rise to an adsorbate clustering effect. Finally, at higher pressures, SO$_2$ molecules further cluster giving rise to the filling of the entire pore volume of the NiBDP structure. This behavior justifies the unusual step shape of the SO$_2$ isotherm. The overall adsorption behavior of NiBDP-1H$_2$O and NiBDP-2H$_2$O is illustrated in Fig. S13 and S14,† respectively. Fig. 6c displays the RDF for SO$_2$/SO$_2$ interaction in NiBDP-0H$_2$O at 298 K. The first characteristic peak was observed at 3.3 Å between S(SO$_2$)–O(SO$_2$), and the second characteristic peak was observed between O(SO$_2$)–O(SO$_2$) at 3.6 Å. These contacts are followed by S(SO$_2$)–S(SO$_2$) at 4.4 Å. RDF analysis of SO$_2$–SO$_2$ interactions pointed out that SO$_2$ molecules are distributed well around the NiBDP-0H$_2$O pore volume.

Furthermore, the enthalpy of adsorption calculated at very low coverage SO$_2$ adsorption is found to be −113.0 kJ mol^{-1} in excellent agreement with the DFT calculated binding energy. These attributes provide a clear indication of achieving an accurate adsorption isotherm at low pressure using this newly derived force field. Indeed, as shown in Fig. 4, the GCMC calculations effectively reproduce the shape of the experimental SO$_2$ adsorption isotherm at low pressure (1 × 10^{-4} bar). NiBDP-

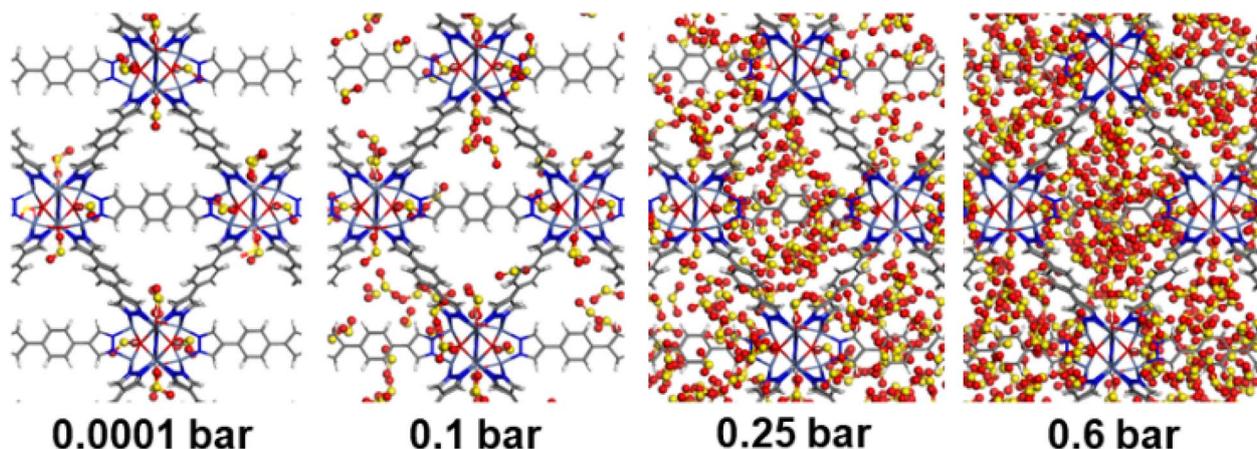**Fig. 5** GCMC simulated adsorption sequence of SO$_2$ in NiBDP-0H$_2$O at 298 K, and at different pressures. SO$_2$ atom color codes: red (O), yellow (S). MOF atom color codes: red (O), gray (C), blue (N), white (H), purple (Ni).
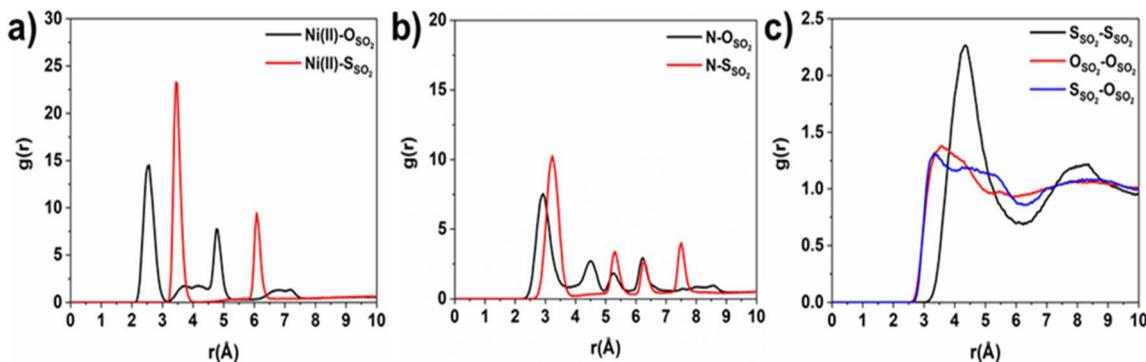
10162 | J. Mater. Chem. A, 2024, **12**, 10157–10165

This journal is © The Royal Society of Chemistry 2024

Fig. 6 Intermolecular radial pair distribution functions of NiBDP-0H$_2$O MOF atoms and adsorbed SO$_2$ molecules were calculated at $P = 0.10$ bar (a and b), and guest SO$_2$–SO$_2$ (c) was calculated at $P = 0.50$ bar.

2H$_2$O shows a distinct SO$_2$ adsorption isotherm profile at low pressure associated with a simulated adsorption enthalpy of -45 kJ. mol^{-1}, more in line with the experimental data that suggests that the activated sample still contains a large concentration of coordinated water. As expected, NiBDP-1H$_2$O is in-between.

A deeper analysis of these simulated isotherms at very low-pressure regions (1×10^{-4} to 0.1 bar) unravels the SO$_2$ adsorption mechanism in all NiBDP-nH$_2$O ($n = 0, 1, 2$) systems. However, depending on the availability of CUS sites in NiBDP frameworks, the amount of SO$_2$ uptake varies, with NiBDP-2H$_2$O, NiBDP-1H$_2$O and NiBDP-0H$_2$O showing 0.00 mmol g^{-1}, 0.55 mmol g^{-1} and 1.12 mmol g^{-1} at 1×10^{-4} bar, respectively. This highlights that the presence of CUS sites in the NiBDP framework enhances SO$_2$ uptake at a very low-pressure domain. Nevertheless, for all three NiBDP MOFs, our GCMC-predicted SO$_2$ isotherms exceed the experimental results above 0.2 bar, which may be attributed to differences in the experimentally and theoretically calculated BET surface area (see above).

Conclusions

In summary, a Ni(II)-based pyrazolate MOF, NiBDP, has been investigated for SO$_2$ adsorption under static conditions. This material exhibits exceptional chemical stability and a maximum SO$_2$ adsorption capacity of 8.48 mmol g^{-1} at 298 K and 1 bar and an unusual step isotherm. Molecular simulations reveal that the SO$_2$ uptake of this material strongly depends on the concentration of Ni CUS sites and the presence of coordinated water molecules with stepwise seeding and clustering of adsorbate molecules. FTIR and *in situ* DRIFTS experiments corroborated the presence of coordinated water molecules and the availability of Ni(II) CUS sites in the structure simultaneously. A microscopic picture of the SO$_2$ adsorption mechanism has thus been gained in line with the unusual adsorption isotherm profile exhibited by this material. Thereby, the study highlights the relevance of robust Ni-pyrazolate MOF materials for high SO$_2$ stability.

Conflicts of interest

There are no conflicts to declare.

Acknowledgements

References

1 M. Sai Bhargava Reddy, D. Ponnamma, K. K. Sadasivuni, B. Kumar and A. M. Abdullah, *RSC Adv.*, 2021, **11**, 12658–12681.

2 S. He, J. Yang, S. Liu, X. Wang, X. Che, M. Wang and J. Qiu, *Chem. Eng. J.*, 2023, **454**, 140202.

3 H. Li, M. Eddaoudi, M. O'Keeffe and O. M. Yaghi, *Nature*, 1999, **402**, 276–279.

4 X. Zheng, H. Zhang, L.-M. Yang and E. Ganz, *Cryst. Growth Des.*, 2021, **21**, 2474–2480.

5 H. Zhang, X. Zheng, L.-M. Yang and E. Ganz, *Inorg. Chem.*, 2021, **60**, 2656–2662.

6 H. Zhang, L.-M. Yang, H. Pan and E. Ganz, *Phys. Chem. Chem. Phys.*, 2020, **22**, 24614–24623.

7 H. Zhang, L.-M. Yang and E. Ganz, *Langmuir*, 2020, **36**, 14104–14112.

8 H. Zhang, C. Shang, L.-M. Yang and E. Ganz, *Inorg. Chem.*, 2020, **59**, 16665–16671.

9 H. Zhang, L.-M. Yang, H. Pan and E. Ganz, *Cryst. Growth Des.*, 2020, **20**, 6337–6345.

10 H. Zhang, L.-M. Yang and E. Ganz, *ACS Sustain. Chem. Eng.*, 2020, **8**, 14616–14626.

11 H. Zhang, L.-M. Yang and E. Ganz, *ACS Appl. Mater. Interfaces*, 2020, **12**, 18533–18540.

12 T. Islamoglu, Z. Chen, M. C. Wasson, C. T. Buru, K. O. Kirlikovali, U. Afrin, M. R. Mian and O. K. Farha, *Chem. Rev.*, 2020, **120**, 8130–8160.

13 V. B. López-Cervantes, J. L. Obeso, A. Yañez-Aulestia, A. Islas-Jácome, C. Leyva, E. González-Zamora, E. Sánchez-González and I. A. Ibarra, *Chem. Commun.*, 2023, **59**, 10343–10359.

This journal is © The Royal Society of Chemistry 2024

J. Mater. Chem. A, 2024, **12**, 10157–10165 | **10163**

14 S. He, J. Yang, S. Liu, X. Wang and J. Qiu, *Adv. Funct. Mater.*, 2023, 2314133.

15 M. Woellner, S. Hausdorf, N. Klein, P. Mueller, M. W. Smith and S. Kaskel, *Adv. Mater.*, 2018, **30**, 1704679.

16 D. Britt, D. Tranchemontagne and O. M. Yaghi, *Proc. Natl. Acad. Sci. U. S. A.*, 2008, **105**, 11623–11627.

17 N. S. Bobbitt, M. L. Mendonca, A. J. Howarth, T. Islamoglu, J. T. Hupp, O. K. Farha and R. Q. Snurr, *Chem. Soc. Rev.*, 2017, **46**, 3357–3385.

18 E. Martínez-Ahumada, M. L. Díaz-Ramírez, M. de J. Velásquez-Hernández, V. Jancik and I. A. Ibarra, *Chem. Sci.*, 2021, **12**, 6772–6799.

19 A. J. Rieth, A. M. Wright and M. Dincă, *Nat. Rev. Mater.*, 2019, **4**, 708–725.

20 K. Tan, S. Zuluaga, H. Wang, P. Canepa, K. Soliman, J. Cure, J. Li, T. Thonhauser and Y. J. Chabal, *Chem. Mater.*, 2017, **29**, 4227–4235.

21 K. Tan, S. Zuluaga, Q. Gong, Y. Gao, N. Nijem, J. Li, T. Thonhauser and Y. J. Chabal, *Chem. Mater.*, 2015, **27**, 2203–2217.

22 R. Colorado-Peralta, J. María Rivera-Villanueva, J. Manuel Mora-Hernández, D. Morales-Morales and L. Ángel Alfonso-Herrera, *Polyhedron*, 2022, **224**, 115995.

23 C. Bao, Q. Niu, Z.-A. Chen, X. Cao, H. Wang and W. Lu, *RSC Adv.*, 2019, **9**, 29474–29481.

24 M. Kurmoo, H. Kumagai, M. Akita-Tanaka, K. Inoue and S. Takagi, *Inorg. Chem.*, 2006, **45**, 1627–1637.

25 S. Zheng, X. Li, B. Yan, Q. Hu, Y. Xu, X. Xiao, H. Xue and H. Pang, *Adv. Energy Mater.*, 2017, **7**, 1602733.

26 V. B. López-Cervantes, D. W. Kim, J. L. Obeso, E. Martínez-Ahumada, Y. A. Amador-Sánchez, E. Sánchez-González, C. Leyva, C. S. Hong, I. A. Ibarra and D. Solis-Ibarra, *Nanoscale*, 2023, **15**, 12471–12475.

27 C. Pettinari, A. Tăbăcaru and S. Galli, *Coord. Chem. Rev.*, 2016, **307**, 1–31.

28 T. He, Z. Huang, S. Yuan, X.-L. Lv, X.-J. Kong, X. Zou, H.-C. Zhou and J.-R. Li, *J. Am. Chem. Soc.*, 2020, **142**, 13491–13499.

29 A. J. Rieth and M. Dincă, *J. Am. Chem. Soc.*, 2018, **140**, 3461–3466.

30 L. M. Rodríguez-Albelo, E. López-Maya, S. Hamad, A. R. Ruiz-Salvador, S. Calero and J. A. R. Navarro, *Nat. Commun.*, 2017, **8**, 14457.

31 N. M. Padial, E. Quartapelle Procopio, C. Montoro, E. López, J. E. Oltra, V. Colombo, A. Maspero, N. Masciocchi, S. Galli, I. Senkovska, S. Kaskel, E. Barea and J. A. R. Navarro, *Angew. Chem., Int. Ed.*, 2013, **52**, 8290–8294.

32 J. Hafner, *J. Comput. Chem.*, 2008, **29**, 2044–2078.

33 P. E. Blöchl, *Phys. Rev. B: Condens. Matter Mater. Phys.*, 1994, **50**, 17953–17979.

34 J. P. Perdew, K. Burke and M. Ernzerhof, *Phys. Rev. Lett.*, 1996, **77**, 3865–3868.

35 S. Grimme, *J. Comput. Chem.*, 2006, **27**, 1787–1799.

36 A. S. Palakkal and R. S. Pillai, *J. Phys. Chem. C*, 2020, **124**, 16975–16989.

37 M. R. Tchalala, P. M. Bhatt, K. N. Chappanda, S. R. Tavares, K. Adil, Y. Belmabkhout, A. Shkurenko, A. Cadiau, N. Heymans, G. De Weireld, G. Maurin, K. N. Salama and M. Eddaoudi, *Nat. Commun.*, 2019, **10**, 1328.

38 L. Wang, T. Maxisch and G. Ceder, *Phys. Rev. B: Condens. Matter Mater. Phys.*, 2006, **73**, 195107.

39 T. A. Manz and N. G. Limas, *RSC Adv.*, 2016, **6**, 47771–47801.

40 T. A. Manz and D. S. Sholl, *J. Chem. Theory Comput.*, 2010, **6**, 2455–2468.

41 T. F. Willems, C. H. Rycroft, M. Kazi, J. C. Meza and M. Haranczyk, *Microporous Mesoporous Mater.*, 2012, **149**, 134–141.

42 K. Gopalsamy, M. Wahiduzzaman, A. Daouli, M. Badawi and G. Maurin, *ACS Appl. Nano Mater.*, 2022, **5**, 15123–15132.

43 E. Haldoupis, J. Borycz, H. Shi, K. D. Vogiatzis, P. Bai, W. L. Queen, L. Gagliardi and J. I. Siepmann, *J. Phys. Chem. C*, 2015, **119**, 16058–16071.

44 J. A. Gee and D. S. Sholl, *J. Phys. Chem. C*, 2015, **119**, 16920–16926.

45 H. Fang, H. Demir, P. Kamakoti and D. S. Sholl, *J. Mater. Chem. A*, 2014, **2**, 274–291.

46 E. Martínez-Ahumada, D. won Kim, M. Wahiduzzaman, P. Carmona-Monroy, A. López-Olvera, D. R. Williams, V. Martis, H. A. Lara-García, S. López-Morales, D. Solis-Ibarra, G. Maurin, I. A. Ibarra and C. S. Hong, *J. Mater. Chem. A*, 2022, **10**, 18636–18643.

47 A. K. Rappe, C. J. Casewit, K. S. Colwell, W. A. Goddard and W. M. Skiff, *J. Am. Chem. Soc.*, 1992, **114**, 10024–10035.

48 M. H. Ketko, G. Kamath and J. J. Potoff, *J. Phys. Chem. B*, 2011, **115**, 4949–4954.

49 P. P. Ewald, *Ann. Phys.*, 1921, **369**, 253–287.

50 J. D. Gale and A. L. Rohl, *Mol. Simul.*, 2003, **29**, 291–341.

51 D.-Y. Peng and D. B. Robinson, *Ind. Eng. Chem. Fundam.*, 1976, **15**, 59–64.

52 B. Widom, *J. Chem. Phys.*, 1963, **39**, 2808–2812.

53 N. Masciocchi, S. Galli, V. Colombo, A. Maspero, G. Palmisano, B. Seyyedi, C. Lamberti and S. Bordiga, *J. Am. Chem. Soc.*, 2010, **132**, 7902–7904.

54 S. Yang, J. Sun, A. J. Ramirez-Cuesta, S. K. Callear, W. I. F. David, D. P. Anderson, R. Newby, A. J. Blake, J. E. Parker, C. C. Tang and M. Schröder, *Nat. Chem.*, 2012, **4**, 887–894.

55 E. López-Maya, C. Montoro, V. Colombo, E. Barea and J. A. R. Navarro, *Adv. Funct. Mater.*, 2014, **24**, 6130–6135.

56 K. V. Kumar, S. Gadipelli, B. Wood, K. A. Ramisetty, A. A. Stewart, C. A. Howard, D. J. L. Brett and F. Rodriguez-Reinoso, *J. Mater. Chem. A*, 2019, **7**, 10104–10137.

57 J. Li, G. L. Smith, Y. Chen, Y. Ma, M. Kippax-Jones, M. Fan, W. Lu, M. D. Frogley, G. Cinque, S. J. Day, S. P. Thompson, Y. Cheng, L. L. Daemen, A. J. Ramirez-Cuesta, M. Schröder and S. Yang, *Angew. Chem., Int. Ed.*, 2022, **61**, e202207259.

58 X. Cui, Q. Yang, L. Yang, R. Krishna, Z. Zhang, Z. Bao, H. Wu, Q. Ren, W. Zhou, B. Chen and H. Xing, *Adv. Mater.*, 2017, **29**, 1606929.

59 Y. Zhang, P. Zhang, W. Yu, J. Zhang, J. Huang, J. Wang, M. Xu, Q. Deng, Z. Zeng and S. Deng, *ACS Appl. Mater. Interfaces*, 2019, **11**, 10680–10688.

60 M. Savage, Y. Cheng, T. L. Easun, J. E. Eyley, S. P. Argent, M. R. Warren, W. Lewis, C. Murray, C. C. Tang,

10164 | *J. Mater. Chem. A*, 2024, **12**, 10157–10165

This journal is © The Royal Society of Chemistry 2024

M. D. Frogley, G. Cinque, J. Sun, S. Rudić, R. T. Murden, M. J. Benham, A. N. Fitch, A. J. Blake, A. J. Ramirez-Cuesta, S. Yang and M. Schröder, *Adv. Mater.*, 2016, **28**, 8705–8711.

61 A. López-Olvera, J. A. Zárate, E. Martínez-Ahumada, D. Fan, M. L. Díaz-Ramírez, P. A. Sáenz-Cavazos, V. Martis, D. R. Williams, E. Sánchez-González, G. Maurin and I. A. Ibarra, *ACS Appl. Mater. Interfaces*, 2021, **13**, 39363–39370.

62 N. Hanikel, X. Pei, S. Chheda, H. Lyu, W. Jeong, J. Sauer, L. Gagliardi and O. M. Yaghi, *Science*, 2021, **374**, 454–459.

63 V. Colombo, S. Galli, H. J. Choi, G. D. Han, A. Maspero, G. Palmisano, N. Masciocchi and J. R. Long, *Chem. Sci.*, 2011, **2**, 1311.

64 A. Nuhnen and C. Janiak, *Dalton Trans.*, 2020, **49**, 10295–10307.

65 F. Salles, G. Maurin, C. Serre, P. L. Llewellyn, C. Knöfel, H. J. Choi, Y. Filinchuk, L. Oliviero, A. Vimont, J. R. Long and G. Férey, *J. Am. Chem. Soc.*, 2010, **132**, 13782–13788.

66 K. I. Hadjiivanov, D. A. Panayotov, M. Y. Mihaylov, E. Z. Ivanova, K. K. Chakarova, S. M. Andonova and N. L. Drenchev, *Chem. Rev.*, 2021, **121**, 1286–1424.

67 K. Tan, P. Canepa, Q. Gong, J. Liu, D. H. Johnson, A. Dyevoich, P. K. Thallapally, T. Thonhauser, J. Li and Y. J. Chabal, *Chem. Mater.*, 2013, **25**, 4653–4662.

68 V. Bon, E. Brunner, A. Pöppl and S. Kaskel, *Adv. Funct. Mater.*, 2020, **30**, 1907847.

69 E. Martínez-Ahumada, M. L. Díaz-Ramírez, H. A. Lara-García, D. R. Williams, V. Martis, V. Jancik, E. Lima and I. A. Ibarra, *J. Mater. Chem. A*, 2020, **8**, 11515–11520.

70 C. C. Zhang, J. Shi, S. Hartlaub, J. P. Palamara, I. Petrovic and B. Yilmaz, *Catal. Commun.*, 2021, **150**, 106273.

71 S. L. Mayo, B. D. Olafson and W. A. Goddard, *J. Phys. Chem.*, 1990, **94**, 8897–8909.

This journal is © The Royal Society of Chemistry 2024

J. Mater. Chem. A, 2024, **12**, 10157–10165 | **10165**